Ocean Sci. Discuss., 10, 619–648, 2013
www.ocean-sci-discuss.net/10/619/2013/
doi:10.5194/osd-10-619-2013

Ocean Science
Discussions
Open Access

Mechanisms of AMOC variability simulated by the NEMO model

V. N. Stepanov and K. Haines

Department of Meteorology, University of Reading, Reading, UK

Received: 7 March 2013 – Accepted: 20 March 2013 – Published: 27 March 2013

Correspondence to: V. N. Stepanov (vlnst@hotmail.com)

Published by Copernicus Publications on behalf of the European Geosciences Union.

Abstract

We have investigated dominant mechanisms of the Atlantic Meridional Overturning Circulation (AMOC) variability at 26.5° N (without the Ekman component) on monthly timescales using 1° and 1/4° NEMO model data. All data were detrended and the seasonal cycle removed. The spatial lead-lag correlations of different hydrodynamic fields with the AMOC time series were calculated.

The analysis shows that the AMOC depends on the strength of wind over the North Atlantic on different time scales. At ∼ 1 yr the January–June difference of mean sea level pressure between high and mid-latitudes in the North Atlantic defines (according to different model runs) 35–50 % of the annual AMOC variability. At interannual time scales ∼ 4 yr after strong (weak) winds over the North Atlantic the AMOC transport becomes higher (lower) by means of an increase (a decrease) in deep water formation in the North Atlantic subpolar gyre. The analysis of the 1/4° NEMO model shows that about 30 % of the AMOC variability is due to density changes in the top 1000 m in the Labrador and Irminger seas occurring about 4 yr early.

1 Introduction

Many model results (see, e.g. Delworth and Greatbatch, 2000; Eden and Willebrand, 2001; Dong and Sutton, 2005; Lohmann et al., 2009a, b; Lazier et al., 2002; Böning et al., 2006; Deshayes and Frankignoul, 2008) show that strong winds over the North Atlantic (characterized by the positive North Atlantic Oscillation (NAO) index) lead to an increase in the AMOC, through an increase in deep water formation in the North Atlantic subpolar gyre, eg. Marshall et al. (2001); Visbeck et al. (2003). Other model results have also suggested that reduction of buoyancy forced deep convection in the subpolar gyre can also lead to a decline in the AMOC (Häkkinen and Rhines, 2004; Bersch et al., 2007).

The other possible mechanism for changing the AMOC is through Ekman pumping changes over the subtropical gyre. Changes in wind stress lead to wind stress curl change impacting on the gyre transports (Eden and Willebrand, 2001; Marshall et al., 2001). The Ocean adjusts to these wind stress curl changes via the westward propagation of Rossby waves associated with anomalies in isopycnal depth and heat content, Schneider et al. (2002); Leadbetter et al. (2007) which may then lead to changes in the AMOC when they interact at the western boundary.

We will investigate these two possible mechanisms of AMOC variability at 26.5° N using analyses of 1° and 1/4° NEMO model data. Two different horizontal resolutions have been used and the AMOC relationships are different. The finer resolution models permit ocean eddies that may be important for the interannual variability of both the ocean heat transport (Volkov et al., 2008), and the AMOC (Biastoch et al., 2008; Kanzow et al., 2009). There is also considerable evidence from different model studies that the adjustment processes are usually faster in higher resolution models (Döscher et al., 1994; Getzlaff et al., 2005; Roussenov et al., 2008; Zhang, 2010; Hodson and Sutton, 2012), likely due to an improved simulation of boundary (Döscher et al., 1994) and coastally trapped (Wang and Mooers, 1976) waves, which can impact the propagation of AMOC anomalies. Therefore boundary wave signals propagate faster in higher resolution models (Döscher et al., 1994; Getzlaff et al., 2005; Roussenov et al., 2008).

The analysis of monthly averaged model results from free model simulation runs at different resolution, were carried out. The Ekman component and seasonal cycle were removed from the model AMOC transport at 26.5° N (henceforth referred to as AMOC-Ek). All model variables were detrended, and the seasonal cycle was also removed.

Section 2 briefly introduces the NEMO model and forcing methods. Section 3 describes the numerical experiments and Sect. 4 presents the results of correlation analyses. Section 5 shows the model relationships between atmospheric and ocean characteristics. Section 6 provides discussion and conclusions about the link between atmospheric processes and the AMOC variability.

2 Model description

The numerical model used is the NEMO coupled ice-ocean model (Madec, 2008) version 2.3, based on the OPA9 ocean model (Madec et al., 1998) and the LIM2.0 sea ice model (Louvain sea Ice Model: Fichefet and Maqueda, 1997; Goosse and Fichefet, 1999), which is a dynamic-thermodynamic model specifically designed for climate studies. The ocean model is a primitive equation z level model making use of the hydrostatic and Boussinesq approximations. The model employs a free surface (Roullet and Madec, 2000) with partial cell topography (Adcroft et al., 1997). The version used here has a tri-polar "ORCA" grid and 46 levels in the vertical, with thicknesses ranging from 6 m at the surface to 250 m at the ocean bottom. The model configuration has a global 1° resolution with a tropical refinement to 1/3° (ORCA1) and a global 1/4° resolution (ORCA025) with horizontal resolution 27.75 km at the equator, 13.8 km at 60° N, and to 10 km in the Arctic Ocean. The configuration has been developed through the DRAKKAR Consortium (Barnier et al., 2007) and uses model parameter settings as defined in (Barnier et al., 2006) and (Penduff et al., 2009). The configuration employs an energy-enstrophy conserving momentum advection scheme (Barnier et al., 2006) and a Laplacian diffusion. Horizontal viscosity is parameterized with a Laplacian operator. Additionally, the ORCA1 configuration makes use of the Gent and McWilliams (1990) mixing parameterization. Vertical mixing is parameterized using a one-equation turbulent kinetic energy scheme (Blanke and Delecluse, 1993). More details may be found in Barnier et al., (2006), and Penduff et al. (2007).

The NEMO model was forced by two atmospheric data sets. The two longest (1958–2004) runs were forced by the hybrid DFS3 (DRAKKAR Forcing Set 3) atmospheric fields, with bulk fluxes calculated as in Large and Yeager (2004). The DFS3 fields have been thoroughly evaluated with the NEMO model at various resolutions and have been shown to provide balanced and physically consistent results (Brodeau et al., 2009). In DFS3, the long- and short-wave radiative fluxes are derived from the CORE dataset (daily means), while the surface winds, temperature and humidity are taken from the

ERA-40 ECMWF reanalysis for 1958–2001, and from ECMWF operational analyses thereafter.

The second set of surface atmospheric forcing for the period 1989–2008 is obtained from ECMWF ERAInterim 6 h reanalysis (Simmons et al., 2007; Dee and Uppala, 2009). The ERAInterim reanalysis provides 10 m wind, 2 m air humidity and 2 m air temperature to compute 6-hourly turbulent air/sea and air/sea-ice fluxes during model integration, using the bulk formula proposed by Large and Yeager (2004). Downwelling short and long wave radiative fluxes and precipitation are also provided by ERAInterim. For all model runs monthly runoffs (Dai and Trenberth, 2002) are applied along the land mask. More details about the model configuration and the simulation results may be found in Barnier et al. (2006), Penduff et al. (2007, 2009), Smith and Haines (2009), Smith et al. (2010), Stepanov et al. (2012) and Haines et al. (2012).

3 Description of numerical experiments

The 1989–2008 period is simulated in the 1° (ORCA1-ERA) model run and also at 1/4° (ORCA025-ERA) model. The experiments are summarized in Table 1. For the ORCA1-ERA experiment the initial conditions are from the World Ocean Atlas 2005 (WOA05) climatology (Boyer et al., 2006) with a cold start in January 1989, i.e. no initial circulation, and then forced with ERA-Interim. The equivalent ORCA025-ERA experiment has been described elsewhere (Haines et al., 2012) as the free control run associated with the reanalysis UR025.3, initiated from a previous 1/4° run driven with hydrographic data assimilation (Smith and Haines, 2009), but run over 1989–2010 forced by ERAInterim forcing.

However the 1989–2010 period is quite short for obtaining robust AMOC variability so we have also used the ORCA025–G70 simulation performed by the DRAKKAR group (2007) that was driven over 1958–2004 by the hybrid interannual forcing DFS3. The same forcings for the same period were also used for the 1° model configuration, presented by Smith and Haines (2009), the ORCA1-R07 model results.

4 Correlations from the NEMO model

The importance of both deep and shallow density distributions to driving the AMOC has been examined from the natural variability of the model. Figure 1 shows the annual timeseries of AMOC-Ek from the four model runs described in the paper. All runs show relatively similar short period variability. The long high resolution run ORCA025-G70 also shows low frequency variability, with a slow rise in AMOC from 1970–1995 with a decline thereafter. The equivalent low resolution run ORCA1-R07 does not show this low frequency variability, and ORCA1-ERA similarly shows no peak in 1995. The shorter ORCA025-ERA run does show more AMOC variations and attempts to reach higher AMOC values around 1995 but the response is more unsteady. The differences between the high resolution runs are due to differences in both the wind forcing, and the initial conditions in 1989. In the high resolution runs the low frequency AMOC variance dominates and so we expect the correlation signals to mainly pick out the processes associated with this low frequency variance.

Figure 2a and c show the correlations of the annual mean AMOC-Ek at 26.5° N with the 1000–3000 m averaged density anomalies in the ORCA1-R07 and ORCA025-G70 models for the 45 yr period 1960–2004 inclusive. The high densities along the western boundary and lower densities on the eastern boundary at 26.5° N indicate stronger vertical shear and hence stronger AMOC. While the eastern spatial patterns are qualitatively similar between the two models, the western correlation patterns are quite different.

Deep layer density correlations from ORCA1-R07 are confined to the subtropical gyre reaching only ∼ 40–45° N on the western boundary, and extending well into the basin interior. These are consistent with Ekman pumped density anomalies in the subtropical gyre propagating to the western boundary and then down to influence 26.5° N. Similar patterns of correlation have been found for monthly variability in long free runs of the HadCM3 coupled model, Hermanson et al. (2013). However in contrast the ORCA025-G70 density correlations are confined to a narrow strip at the western

boundary of the subtropical gyre, but this strip extends up into the subpolar gyre where the influence spreads and fills the Labrador and Irminger seas. These correlations are consistent with dense water formation in the high latitudes influencing density down the western boundary, e.g. see Hodson and Sutton (2012). In particular this associates the low frequency signals seen in Fig. 1 with a Labrador Sea origin. There are weaker correlations with upper Labrador sea densities above 1000 m also, which extend partway down the western boundary and then terminate (Fig. 2b, d). This probably reflects the extent of advected denser water anomalies at these upper levels which terminate at the intergyre boundary. The ORCA1-R07 shows some correlation between AMOC-Ek and dense water in the Labrador Sea, however the area of correlations is much smaller in Fig. 2, it is not clearly connected with the western boundary, and these correlations disappear if only 20 yr of data (1989–2008) are used whereas Labrador Sea correlations are still robust for 20 yr of data in the higher resolution model.

The fact that AMOC-Ek at 26° N is not robustly correlated to deep Labrador Sea densities in the 1° model suggests that the coarse model may not adequately resolve the boundary wave propagation mechanism (this agrees with Hodson and Sutton (2012) who show that the timescale of deep ocean evolution of the western boundary anomaly is sensitive to model resolution). Figure 2e,f show ORCA025-G70 correlations now using monthly data. Most of the signals are similar to the annual-only correlations in Fig. 2c, d but with reduced correlations presumably due to more noise at the sub-annual frequency. However in the top 1000 m there are interesting differences at the western boundary. With monthly time scales there is a correlated signal stretching from 40° N–26° N very close to the western boundary, while this signal is absent in the annual correlations. This signal is still present with high pass filtering to timescales of 6 months or less, Fig. 2g, h, and so we take this to be the signal of fast boundary waves triggered by Ekman pumping in the subtropical gyre, again similar to the HadCM3 results in Hermanson et al. The difference between the 1° and 1/4° model correlation patterns in the subtropics is likely due to higher mesoscale density variability in the 1/4° model compared to 1°. Figure 3 shows the standard deviation of monthly density

variability in the 2 models at 1000–3000 m and in the top 1000 m. Areas of higher density variability at higher resolution will mask correlations from Ekman pumped density anomalies throughout the subtropical gyre. We can see an area with high correlation in the subtropics to the south of 30° N, Fig. 2 (b, d), where the density variability is lower, Fig. 3c, d, both for the ORCA1-R07 and ORCA025-G70 runs, while to the north of 30° N the correlation coefficients are smaller (Fig. 2b, d) since mesoscale model variability is high here (Fig. 3c, d). We can see the same patterns for model correlations and density variability for the 1000–3000 m layer (Fig. 2a, c and Fig. 3a, b).

There is also a substantial difference in dense water formation in the Labrador and Irminger seas reproduced by the 1° and 1/4° NEMO models. Figure 4 presents annual time series of AMOC-Ek transport anomaly at 26.5° N (thick red dashed line) and density anomaly averaged over the Labrador and Irminger seas between 50–35° W and 45–60° N (thick blue dashed line), in the 1000–3000 m layer (Fig. 4a), and in the top 1000 m (Fig. 4b) from ORCA025-G70 (the area is marked by a red rectangle in Fig. 3d). The deep layer shows the highest correspondence at zero lag (correlation 0.75), while in the top 1000 m the AMOC lags by 4 yr (correlation 0.64). We conclude that in the ORCA025-G70 model about 4 yr is needed for the upper ocean signal to reach deeper layers in the Labrador and Irminger seas and then this deeper density variability rapidly influences AMOC transports at 26.5° N with zero lag, Fig. 4a.

The thin solid lines (red and blue) in Fig. 4a, b show the same quantities from the ORCA1-R07 model. The Labrador Sea variability in R07 is very similar to that in G70 in the top 1000 m, especially during the larger changes around 1995, presumably reflecting the same surface forcing. However in the deeper layers the amplitude of density anomalies in R07 is considerably reduced, despite the same surface forcing hence, the stratification in the Labrador and Irminger seas for the 1° and 1/4° NEMO models are different resulting in different processes of deep water formation in the two models. We suggest that the different circulations in the subpolar gyre at the different resolutions allows dense water to be more easily exported from the Labrador and Irminger seas at upper levels, thereby reducing the amount of the deepest dense

waters formed. Another mechanism that might be enabling this is the operation of the Gent and McWilliams (1990) eddy parametrisation scheme which is implemented in ORCA1-R07 but not in ORCA025-G70. This is a second reason why the AMOC-Ek transport anomalies at 26.5° N in ORCA1-R07 would show reduced correlations with the subpolar gyre.

5 Linkage between atmospheric and ocean characteristics

If the long term AMOC variability due to deep water density variability in the Labrador and Irminger seas is discounted then the AMOC variability in the 1° and 1/4° models in Fig. 1 are fairly similar, presumably reflecting direct wind generated variability. The amplitude of interannual ORCA025-G70 AMOC variability after subtraction of the low frequency component, from 1963 onwards decreases from 0.65 to 0.45 Sv and is very comparable to the ORCA1-R07 timeseries variability (0.4 Sv). However the high frequency R07 variability at timescales < 3 months is 50 % less than in G70 showing that both the lowest and highest frequency AMOC variability are inadequately reproduced by the 1° model.

Since the vertical resolution and external forcings in the 1° and 1/4° models are identical, the AMOC differences can only be due to horizontal resolution and the Gent and McWilliams (1990) eddy parametrisation scheme which is implemented in the 1° model. A finer resolution results in more intense gyre circulation, particularly near the western boundary and in the Labrador Sea, as shown in the barotropic streamfunctions in Fig. 5a, b. Figure 5a, b show that the subpolar gyre circulation in ORCA025 can also penetrate farther to the south along the western boundary via the subpolar cyclonic circulation, compared to ORCA1. This stronger subpolar gyre circulation is also associated with a much stronger mean AMOC (compare Fig. 5c, d).

The higher frequency monthly ORCA1-R07 and ORCA025-G70 time series are not obviously correlated with the NAO-index (the correlation coefficients are not statistically significant), although the variability is still likely to show some dependence upon wind

forcing. Figure 6 shows correlation maps of the average January–June mean sea level pressures with annual mean AMOC transport from ORCA1-ERA (a) and ORCA025-ERA (b), for 1989–2008 (similar patterns are obtained with the longer ORCA1-R07 and ORCA025-G70 time series, not shown). Higher values of AMOC transport correspond to higher sea level pressures over most of the subpolar gyre and particularly the Labrador sea, and lower pressure over the subtropical gyre, i.e. weaker westerly winds are associated with higher AMOC transports. Figure 6c shows the AMOC-Ek transports from all model runs from 1989 onwards, and the January–June mean pressure difference between high and mid latitudes, ΔPa (at the points marked by black crosses on Fig. 6b). The ORCA1-R07, ORCA025-G70 and ORCA025-ERA annual AMOC transports are correlated with ΔPa with coefficients 0.7, 0.7 and 0.6, respectively (all coefficients being statistically significant at 95 %). The January–June mean NAO index (with reversed sign, referred to as NAO^-) is shown as a red dashed line on Fig. 6c. The ΔPa and NAO^- variability are now correlated at 0.6.

Figure 6d shows the January–June mean NAO index (solid line) and the annual Gulf Stream north wall index (GSNW index) from http://www.pml-gulfstream.org.uk (dashed line) after high-pass filtering for periods shorter than 12 months. The GSNW index (see, e.g. Taylor and Stephens, 1998) characterizes the latitude of the Gulf Stream front and describes the north-south shifts of the Gulf Stream. The January–June mean NAO index is correlated with the GSNW index with a significant coefficient of about 0.32 (unfiltered data are correlated with a coefficient of 0.5). A low NAO index corresponds to a southerly position of the Gulf Stream, which means greater southward penetration of the cold Labrador Sea water at the western boundary of the subpolar gyre near 40° N. This southward pulse can excite baroclinic boundary waves that propagate south along the western boundary resulting in cooling and a higher AMOC (in accordance with Fig. 2f, h). It is in agreement with ORCA025-G70 results. The leading EOF1 mode of monthly temperature anomalies at the western boundary of the North Atlantic after high-pass filtering for periods shorter than 12 months is presented in Fig. 6e, and the time series of its normalized principal component PC1 is shown by the red line

on Fig. 6d. A cross-correlation analysis between PC1 and the GSNW index at zero lag for 1966–2004 gives a correlation of 0.34. The EOF1 pattern shown in Fig. 6e shows a cell of warm (cold) water near 35N in the top ∼ 800 m when the Gulf Stream shifts to the north (south). The position of this cell is coincident with the maximum model high frequency (shorter than 12 month) temperature variability at the western boundary (Fig. 6f). This mode explains about 21 % of the total temperature variability at the western boundary. If high-pass filtering of the temperature variability at the western boundary does not remove the frequency band corresponding to periods of 12–48 months, the value of correlation coefficient between PC1 and GSNW index significantly decreases. Therefore we can conclude that the link between the north-south shifts of the Gulf Stream and temperature change at the western boundary is fast and it is likely due to boundary wave and the response that can be seen within 1 yr.

Figure 6g, h shows ORCA025-G70 correlations with AMOC-Ek at 26.5° N using monthly (g) and annual (h) data after high-pass filtering for periods shorter than 12 months. The correlations between high frequency AMOC-Ek at 26.5° N and density at the western boundary show that the density signal from 35N can influence the AMOC: there is a significant correlation between AMOC-Ek at 26.5° N and the western boundary density at 35N from the surface to the deep layers, which is also seen to the south of 35° N below 1000 m (Fig. 6g–h). Most of the monthly signals are similar to the annual correlations but correlations are smaller, presumably due to more noise at the sub-annual frequency.

Another wind driven mechanism that could drive AMOC-Ek variability is Ekman pumping changes in the subtropical gyre. Ocean circulation theories predict that the position of the Gulf Stream and the subpolar-subtropical front is defined by the line of zero Ekman pumping (e.g. see Parsons, 1969; Veronis, 1973; Pedlosky, 1987). So to a first approximation we can assume that a region with maximal wind stress curl moves southward for a persistent low NAO index. This strengthening in Ekman downwelling will be propagated to the western boundary via forced Rossby waves resulting in cooling near the western boundary (e.g. see Leadbetter et al., 2007). The signal

propagates to the west with typical speed of 2 cm s^{-1}, consistent with a first baroclinic mode (Schneider et al., 2002). A lag between wind stress and changes near the western boundary of less than 1 year, would involve wind variability within 600 km of the western boundary.

After applying low-pass filtering for periods longer than 48 months to the NAO-index and the ORCA025-G70 AMOC-Ek time series we get a positive correlation, with the NAO leading the AMOC-Ek by 48 months (Fig. 4c). This lag is in agreement with Fig. 4b showing the same lag time between AMOC transport and density variability in the top 1000 m, and is also consistent with Robson et. al (2012) as well as other observations. For example, after the NAO index reached its peak values in the early 1990s a large layer of anomalously cold Labrador sea water was formed (Yashayaev et al., 2007) due to increased deep convection in the Labrador sea, particularly in the years 1990–1993 (Lazier et al., 2002).

We conclude that in the ORCA025-G70 run about 30 % of the total interannual variability in AMOC-Ek transport is due to dense water formation in the Labrador and Irminger seas, and this variability in turn depends on the wind strength over the subpolar gyre 4 yr before, acting to deepen Labrador Sea convection. Another 35–50 % of the AMOC variability (based on the correlation coefficients between ΔPa and AMOC-Ek obtained from all model runs) is described by January–June sea level pressure differences between high and mid-latitudes over the North Atlantic (in other words to changes in the NAO index). The AMOC fluctuations in ORCA025-G70 have more high frequency variability compared to ORCA1-R07 due to better resolution of fast mesoscale processes: either processes occurring in the subtropical gyre near the western boundary, or better transmission across latitudes via western boundary waves.

6 Summary and discussion

We have analysed results from 1° and 1/4° NEMO ocean models and have found that model AMOC transport substantially depends on the strength of wind over the North

Atlantic through different mechanisms at different time scales. At short time scales of about 1 yr a weaker zonal wind over the North Atlantic (that is characterized by the January–June difference of mean sea level pressure between high and mid-latitudes in the North Atlantic) leads to an increase in the annual AMOC. This is due to the southward shift of the Gulf Stream front that either via an enhanced transport of the cold Labrador Sea water occurring at the western boundary of the subpolar gyre near 40° N triggering western boundary wave propagation, or via Ekman forced downwelling Rossby waves (Schneider et al., 2002; Leadbetter et al., 2007) lead to the intensification of the AMOC.

At this time scale, according to the values of correlation coefficients between January–June mean sea level pressure and AMOC transports from all model runs, about 35–50 % of the AMOC variability can be explained by changes of January–June pressure difference between high and mid-latitudes over the North Atlantic. At longer interannual time scales strong winds over the subpolar gyre (with NAO-index as a measure of the wind strength) leads to an increase in the AMOC by means of an increase in deep water formation in the North Atlantic subpolar gyre. According to model results the change of the top 1000 m density lead the AMOC change by about 4 yr, while the fluctuations of deep layer density are correlated with the AMOC transport with zero lag, but this driving mechanism only works in the higher resolution model. Our analysis shows that about 30 % of the AMOC variability is due to the density change in the top 1000 m in the Labrador and Irminger seas 4 yr earlier.

Figure 7 shows 4 yr lagged correlations of the annual AMOC-Ek at 26.5° N with the top 1000 m averaged density anomalies (a) and sea level (b) in the ORCA025-G70 model, for the 45 yr period 1960–2004 inclusive. For ease of comparison the correlations between AMOC-Ek and sea level are multiplied by −1. The correlation patterns are very similar suggesting that sea level variability can be used as a proxy for the top 1000 m averaged density variability near the western boundary and particularly in the Labrador Sea, that is most highly correlated with AMOC variability (Fig. 2d, f).

Comparing Figs. 7a and 2d we can see the strengthening of higher latitude correlations when introducing the 4 yr lag.

The above correlations are consistent with the rapid warming of the subpolar gyre of the North Atlantic in the mid-1990s which followed a prolonged positive phase of the NAO with a sudden switch to a strongly negative NAO index in 1995–1997. Robson et al. (2012) suggest that both these factors led to high northward meridional heat transports causing the warming.

Numerical experiments with the 1° model show that if the AMOC transport increases at some subtropical latitude (e.g. at 26.5° N by means of the assimilation of data near the western boundary from the RAPID array, Stepanov et al., 2012), this leads to heat transport increase during 2 yr, warming the area of subtropical gyre to the north, particularly along the Gulf Stream path. Large changes in ocean heat content develop at higher latitudes, in particular around the water formation areas of the Labrador and Irminger seas. This warming results in the increase of the stratification of the water column in the top 800 m layer in the mid/high latitudes making it less susceptible to wintertime convection. As a result the AMOC transport decreases after 2 yr due to this negative feedback on water distributions at higher latitudes. Thus, the decline in the AMOC can be driven by a preceding increase in the northward heat transport (that is highly correlated with the AMOC transport), and according to the model estimation the lag between temperature changes in the northern (southern) part of subtropical (polar) gyre and AMOC changes is about of 2 yr. Figure 8 confirms this lag relationship. In Fig. 8 the Atlantic Multidecadal Oscillation timeseries (AMO, see http://www.esrl.noaa.gov/psd/data/correlation/amon.us.data) is shown as a dashed line. The AMO characterises the change in average sea surface temperature (SST) in the Northern Atlantic. One can see that if SST in the North Atlantic reaches some local maximum, then it drops during the next about of 2 yr.

Thus, if we assume that there is a lag of 2 yr between the temperature changes in the North Atlantic and the AMOC change at 26.5° N, and a lag of 4 yr between the long-term variability of the AMOC and NAO index (Fig. 4c), then we might expect some

correlation between the NAO and AMO indices (see Fig. 6c) after a lag ∼ 6 yr. Figure 8 shows the result of a multiple regression analysis (henceforth NAO-AMOC) that allows to build a regression equation of the form:

NAO – AMOC = 0.28 × NAO – Long (with 6 yr lag) – 0.22 × NAO – Short,

where NAO-Long is the NAO index after low-pass filtering for periods longer than 60 months; NAO-Short is NAO index after low-pass filtering for periods longer than 18 months. The NAO-AMOC and AMO are significantly correlated with a correlation coefficient of ∼ 0.5, i.e. the NAO-AMOC accounts for ∼ 25 % of the AMO variability, representing AMOC variability captured by the NAO index.

The mechanisms of AMOC variability considered in this paper are in agreement with the results obtained by other authors: strong winds over the North Atlantic lead to an increase in turbulent fluxes (Marshall et al., 2001; Visbeck et al., 2003) that increases deep water formation in the North Atlantic subpolar gyre resulting in higher values of the AMOC. On the other hand the reduction of the buoyancy forced deep convection (Häkkinen and Rhines, 2004; Bersch et al., 2007) due to weaker winds or an increase in the northward heat transport by the ocean can lead to a decline in the AMOC (Fig. 4).

It was also shown that different horizontal model resolutions substantially influence the simulation of processes occurring at the western boundary: western boundary waves are reproduced better in higher resolution models resulting in faster propagation of AMOC anomaly signals. As a result, with high resolution models we are able to reveal the fast impact of deep water formation in the Labrador and Irminger seas on the AMOC transport.

Acknowledgements. This work was supported by the NCEO and the RAPID-Watch Valor projects.

References

Adcroft A., Hill C., and Marshall J.: Representation of topography by shaved cells in a height coordinate ocean model, Mon. Weather Rev., 125, 2293–2315, 1997.

Barnier, B. and the DRAKKAR Group: Eddy-permitting ocean circulation hindcasts of past decades, Clivar Exchanges, 12, 8–10, 2007.

Barnier, B., Madec, G., Penduff, T., Molines, J. M., Treguier, A. M., Le Sommer, J., Beckmann, A., Biastoch, A., Böning, C., Dengg, J., Derval, J., Durand, E., Gulev, S., Remy, E., Talandier, C., Theetten, S., Maltrud, M., McClean, J., and De Cuevas, B.: Impact of partial steps and momentum advection schemes in a global ocean circulation model at eddy-permitting resolution, Ocean Dynam., 56, 6543–567, doi:10.1007/s10236-006-0082-1, 2006.

Bersch, M., Yashayaev, I., and Koltermann, K.: Recent changes of the thermohaline circulation in the subpolar north atlantic, Ocean Dynam., 57, 223–235, 2007.

Blanke, B. and Delecluse, P.: Variability of the tropical Atlantic Ocean simulated by a general circulation model with two different mixed-layer physics, J. Phys. Oc., 23, 1363–1388, 1993.

Böning, C., Scheinert, M., Dengg, J., Biastoch, A., and Funk, A.: Decadal variability of subpolar gyre transport and its reverberation in the North Atlantic overturning, Geophys. Res. Lett, 33, L21S01, doi:10.1029/2006GL026906, 2006.

Boyer, T. P., Garcia H. E., Johnson D. R., Locarnini R. A., Mishonov A. V., Pitcher M. T., Baranova O. K., and Smolyar I. V.: World Ocean Database 2005, NOAA Atlas NESDIS 60, edited by: Levitus, S., US Gov. Print. Off., Washington DC, 190 pp., 2006.

Brodeau, L., Barnier, B., Treguier, A. M., Penduff, T., and Gulev, S.: An ERA40-based atmospheric forcing for global ocean circulation models, Ocean Model., 31, 88–104, doi:10.1016/j.ocemod.2009.10.005, 2009.

Cunningham, S. A., Kanzow, T., Rayner, D., Baringer, M. O., Johns, W. E., Marotzke, J., Longworth, H. R., Grant, E. M., Hirschi, J. J.-M., Beal, L. M., Meinen, C. S. and Bryden, H. L.: Temporal Variability of the Atlantic Meridional Overturning Circulation at 26.5° N, Science, 317, 935–938, 2007.

Dai, A. and Trenberth, K. E.: Estimates of freshwater discharge from continents: latitudinal and seasonal variations, J. Hydrometeorol., 3, 660–687, 2002.

Dee, D. P. and Uppala, S.: Variational bias correction of satellite radiance data in the ERA-Interim reanalysis, Q. J. R. Meteorol. Soc., 135, 1830–1841, 2009.

Delworth, T. and Greatbatch, R.: Multidecadal thermohaline circulation variability driven by atmospheric surface flux forcing, J. Climate, 13, 1481–1495, 2000.
Deshayes, J. and Frankignoul, C.: Simulated variability of the circulation in the North Atlantic from 1953 to 2003, J. Climate, 21, 4919–4933, doi:10.1175/2008JCLI1882.1, 2008.
Dong, B. and Sutton, R. T.: Mechanism of interdecadal thermohaline circulation variability in a Coupled ocean–atmosphere GCM, J. Climate, 18, 1117–1135, doi:10.1175/JCLI3328.1, 2005.
Döscher, R., Böning, C., and Herrmann, P.: Response of circulation and heat transport in the North Atlantic to changes in thermohaline forcing in northern latitudes: a model study, J. Phys. Oceanogr., 24, 2306–2320, 1994.
DRAKKAR Group: Eddy-permitting ocean circulation hindcasts of past decades, CLIVAR Exchanges, 42, 12, 8–10, 2007.
Eden, C. and Willebrand, J.: Mechanism of interannual to decadal variability of the North Atlantic Circulation., J. Climate, 14, 2266–2280, 2001.
Fichefet, T. and Maqueda M.: Sensitivity of a global sea ice model to the treatment of ice thermodynamics and dynamics, J. Geophys. Res., 102, 12609–12646, 1997.
Gent, P. R. and McWilliams, J. C.: Isopycnal mixing in ocean circulation models, J. Phys. Oc., 20, 150–155, 1990.
Getzlaff, J., Böning, C., Eden, C., and Biastoch, A.: Signal propagation related to the North Atlantic overturning, Geophys. Res. Lett., 32, L09602, doi:10.1029/2004GL021002, 2005.
Goose, H. and Fichefet, T.: Importance of ice-ocean interactions for the global ocean circulation: a model study, J. Geophys. Res., 104, 23337–23355, 1999.
Grist, J. P., Josey, S. A., Marsh, R., Good, S. A., Coward, A. C., de Cuevas, B. A., Alderson, S. G., New, A. L., and Madec, G.: The roles of surface heat flux and ocean heat transport convergence in determining Atlantic Ocean temperature variability, Clim. Dynam., 60, 771–790, doi:10.1007/s10236-010-0292-4, 2010.
Haines, K., Valdivieso, M., Zuo, H., and Stepanov, V. N.: Transports and budgets in a 1/4° global ocean reanalysis 1989–2010, Ocean Sci., 8, 333–344, doi:10.5194/os-8-333-2012, 2012.
Häkkinen, S. and Rhines, P.: Decline of Subpolar North Atlantic circulation during the 1990s, Science, 304, 555–559, doi:10.1126/science.1094917, 2004.
Hermanson, L., Dunstone, N., Haines, K. K., Robson, J., Smith, D., and Sutton, R.: Indirectly assimilating Atlantic 26° N transport into the UK Met Office Decadal Prediction System, Q. J. Roy. Met. Soc., submitted, 2011.

Hodson, D. L. R. and Sutton, R. T.: The impact of resolution on the adjustment and decadal variability of the Atlantic meridional overturning circulation in a coupled climate model, Clim. Dynam., 39, 3057–3073, ISSN 1432-0894, doi:10.1007/s00382-012-1309-0, 2012.
Ingleby, B. and Huddleston, M.: Quality control of ocean temperature and salinity profiles–historical and real-time data, J. Mar. Syst., 65, 158–175, 2007.
Large, W. G. and Yeager, S. G.: Diurnal to decadal global forcing for ocean and sea-ice models: the data sets and flux climatologies, Technical Report TN-460+STR, NCAR, 105 pp., 2004.
Lazier, J., Hendry, R., Clarke, A., Yashayaev, I., and Rhines, P.: Convection and restratification in the Labrador Sea, 1990–2000, Deep-Sea Res. Pt. I, 49, 1819–1835, 2002.
Lohmann, K., Drange, H., and Bentsen, M.: Response of the North Atlantic subpolar gyre to persistent North Atlantic oscillation like forcing, Clim. Dynam., 32, 273–285, doi:10.1007/s00382-008-0467-6, 2009a.
Lohmann, K., Drange, H., and Bentsen, M.: A possible mechanism for the strong weakening of the north atlantic subpolar gyre in the mid-1990s, Geophys. Res. Lett., 36, L15602, doi:10.1029/2009GL039166, 2009b.
Madec, G.: NEMO reference manual, ocean dynamics component: NEMO-OPA, Preliminary version, Note du Pole de modélisation, Institut Pierre-Simon Laplace (IPSL), France, No 27 ISSN No 1288–1619, 2008.
Madec, G., Delecluse, P., Imbard, M., and Levy, C.: OPA 8.1 general circulation model reference manual. Notes de l'IPSL, University P. et M. Curie, B102 T15-E5, No. 11, Paris, 91 pp., 1998.
Marsh, R., Josey, S., De Cuevas, B., Redbourn, L., and Quartly, G.: Mechanisms for recent warming of the north atlantic: insights gained with an eddy-permitting model, J. Geophys. Res., 113, C04031, doi:10.1029/2007JC004096, 2008.
Marshall, J., Johnson, H., and Goodman, J.: A study of the interaction of the North Atlantic oscillation with ocean circulation, J. Climate, 14, 1399–1421, doi:10.1175/1520-0442(2001)014, 2001.
Parsons, A. T.: A two-layer model of Gulf Stream separation, J. Fluid Mech., 39, 511–528, 1969.
Pedlosky, J.: On Parson's model of the ocean circulation, J. Phys. Oceanogr., 17, 1571–1582, 1987.
Penduff, T., Le Sommer, J., Barnier, B., Treguier, A.-M., Molines, J.-M., and Madec, G.: Influence of numerical schemes on current-topography interactions in 1/4° global ocean simulations, Ocean Sci., 3, 509–524, doi:10.5194/os-3-509-2007, 2007.

Penduff, T., Juza, M., Brodeau, L., Smith, G. C., Barnier, B., Molines, J.-M., Treguier, A.-M., and Madec, G.: Impact of global ocean model resolution on sea-level variability with emphasis on interannual time scales, Ocean Sci., 6, 269–284, doi:10.5194/os-6-269-2010, 2010.

Reverdin, G.: North atlantic subpolar gyre surface variability (1895–2009), J. Climate, 23, 4571–4584, doi:10.1175/2010JCLI3493.1, 2010.

Robson, J., Sutton, R., Lohmann, K., Smith, D., and Palmer, M. D.: Causes of the rapid warming of the North Atlantic Ocean in the mid-1990s, J. Climate, 25, 4116–4134, doi:10.1175/JCLI-D-11-00443.1, 2012.

Roussenov, V., Williams, R., Hughes, C., and Bingham, R.: Boundary wave communication of bottom pressure and overturning changes for the north atlantic, J. Geophys. Res, 113, C08042, doi:10.1029/2007JC004501, 2008.

Roullet, G. and Madec G.: Salt conservation, free surface, and varying levels: a new formulation for ocean general circulation models, J. Geophys. Res., 105, 23927–23942, 2000.

Sarafanov, A., Falina, A., Sokov, A., and Demidov, A.: Intense warming and salinification of intermediate waters of southern origin in the eastern subpolar North Atlantic in the 1990s to mid-2000s, J. Geophys. Res, 113, C12022, doi:10.1029/2008JC004975, 2008.

Simmons, A., Uppala S., Dee, D., and Kobayashi S.: ERA-Interim: New ECMWF reanalysis products from 1989 onwards, ECMWF Newsletter, 110, 25–35, 2007.

Smith, G. C. and Haines K.: Evaluation of the S(T) assimilation method with the Argo dataset, Q. J. R. Meteorol. Soc., 135, 739–756, 2009.

Stepanov, V. N., Haines, K., and Smith, G. C.: Assimilation of RAPID observations into an ocean model, Q. J. Roy. Meteorol. Soc., 138, 2105–2117, doi:10.1002/qj.1945, 2012.

Taylor H. and Stephens, J. A.: The North Atlantic oscillation and the latitude of the Gulf Stream, Tellus, 50A, 134–142, 1998.

Veronis G.: Model of world ocean (I), wind-driven, two-layer, J. Mar. Res., 31, 228–288, 1973.

Visbeck, M., Chassignet, E., Curry, R., Delworth, T., Dickson, B., and Krahmann: The ocean's response to North Atlantic oscillation variability, in: The North Atlantic Oscillation: Cinematic Significance and Environmental Impact, Amer. Geophys. Union, 113–146, 2003.

Wang, D. P. and Mooers, C. N. K.: Coastal-trapped waves in a continuously stratified ocean, J. Phys. Oceanogr., 6, 853–863, 1976.

Yashayaev, I., Bersch, M., and Van Aken, H. M.: Spreading of the Labrador Sea water to the Irminger and Iceland basins, Geophys. Res. Lett., 34, L10602, doi:10.1029/2006GL028999, 2007.

Zhang, R.: Latitudinal dependence of Atlantic meridional overturning circulation (AMOC) variations, Geophys. Res. Lett., 37, L16703, doi:10.1029/2010GL044474, 2010.

Table 1. A description of experiments.

No	Experiment	Description
1	ORCA1-ERA	Control 1° NEMO simulation forced with ERAInterim and initialised from 1989 from WOA05 climatology
2	ORCA025-ERA	Control 1/4° NEMO forced with ERAInterim; the initial ocean and sea ice states are taken from previous ocean reanalysis; see Haines et al. (2012)
3	ORCA1-R07	Control 1° NEMO simulation forced with the hybrid interannual forcing DFS3 during 1958–2004
4	ORCA025-G70	Control 1/4° NEMO simulation forced with the hybrid interannual forcing DFS3 during 1958–2004

Table 1 gives a definition of all the experiments used in this paper.

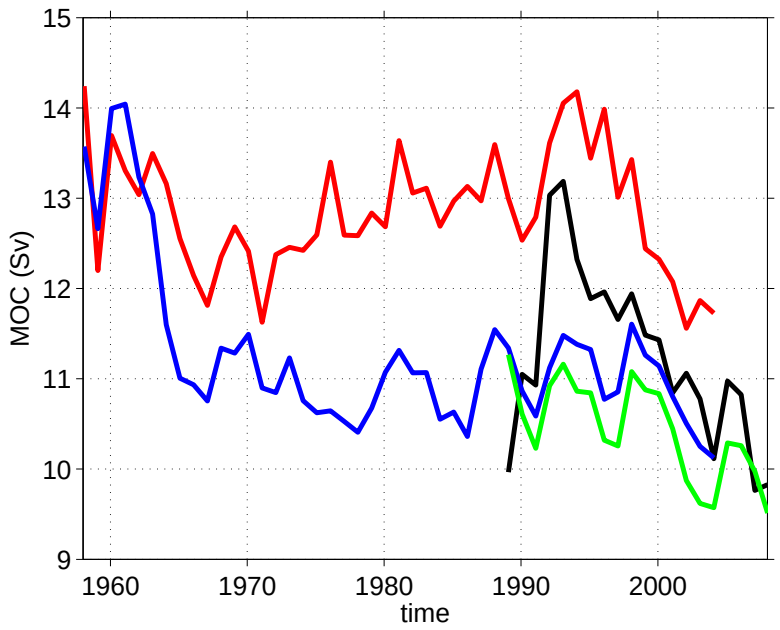

Fig. 1. Timeseries of annual mean AMOC-Ek variability for the 4 model runs studied in this paper. ORCA025-G70 (red), ORCA1-R07 (blue), ORCA025-ERA (black), and ORCA1-ERA (green).

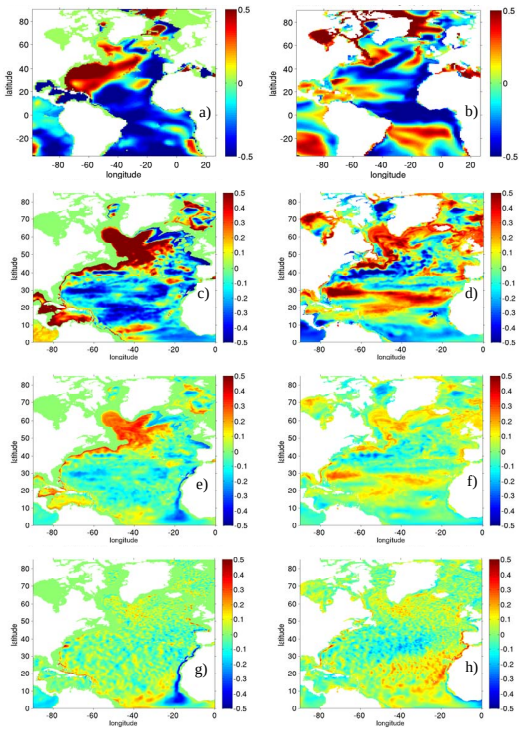

Fig. 2. Correlations of the annual AMOC-Ek at 26.5° N with the 1000–3000 m **(a, c)** and the top 1000 m **(b, d)** averaged density anomalies in ORCA1-R07 **(a, b)** and ORCA025-G70 **(c, d)** models, for the 45 yr period 1960–2004 inclusive. **(e, f)** and **(g, h)** – the same as **(c, d)** but calculated from monthly data and data after high-pass filtering with periods shorter than 6 months, respectively.

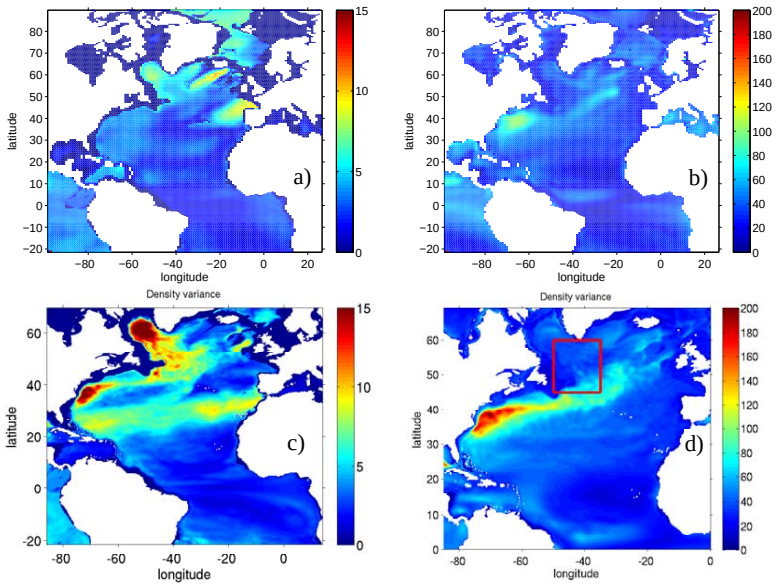

Fig. 3. The standard deviations of the monthly density (in g m^{-3}) averaged on the 1000–3000 m **(a, c)** and the top 1000 m **(b, d)** layers in ORCA1-R07 **(a, b)** and ORCA025-G70 **(c, d)** models (for the 45 yr period 1960–2004 inclusive). Also shown on the right bottom panel by red rectangle is the region that is used to calculate density anomaly (area between 50–35° W and 45–60° N).

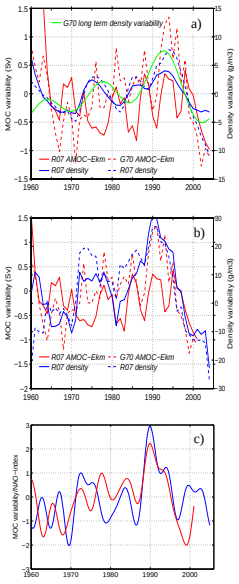

Fig. 4. Annual time series of AMOC-Eks transport anomaly at 26.5° N (red) and density anomaly (blue) averaged over the Labrador and Irminger seas (between 50–35° W and 45–60° N) in 1000–3000 m layer **(a)** and in the top 1000 m **(b)**. Thin solid and thick dashed lines correspond to ORCA1-R07 and ORCA025-G70 runs, respectively. Long term (after use of low-pass filter with periods longer than 13 yr) ORCA025-G70 density variability in 1000–3000 m layer is shown by green solid thick line in **(a)**. The AMOC graphs on **(b)** lags at 48 months compared to density curves; **(c)** – NAO-index (blue) and AMOC-Eks variability at 26.5° N (red) after low-pass filtering with periods longer than 48 months and normalised to unit variance to have zero mean and a standard deviation of one, here AMOC time series is shifted 48 months back relative to the NAO-index.

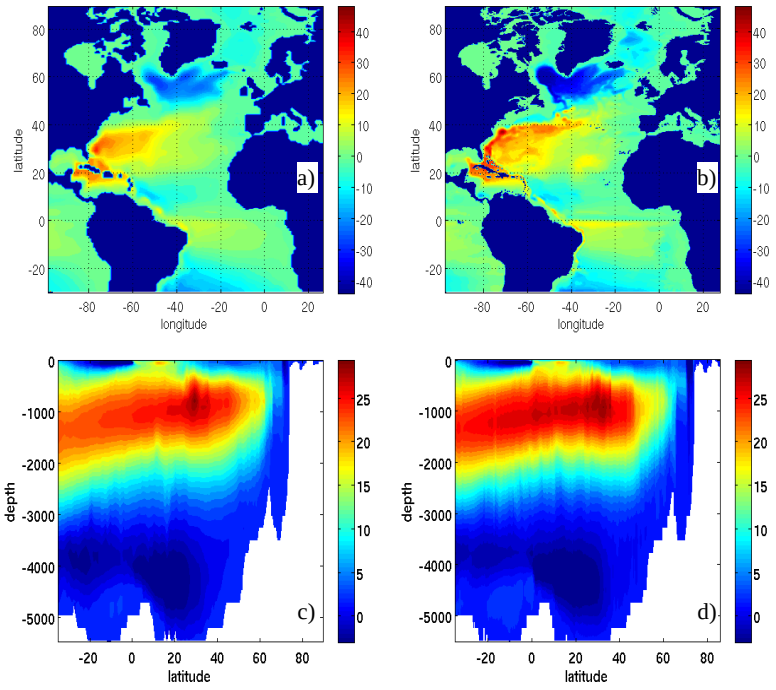

Fig. 5. 45 yr averaged barotropic and AMOC stream functions (in Sv) for ORCA1-R07 **(a, c)** and ORCA025-G70 **(b, d)**, respectively.

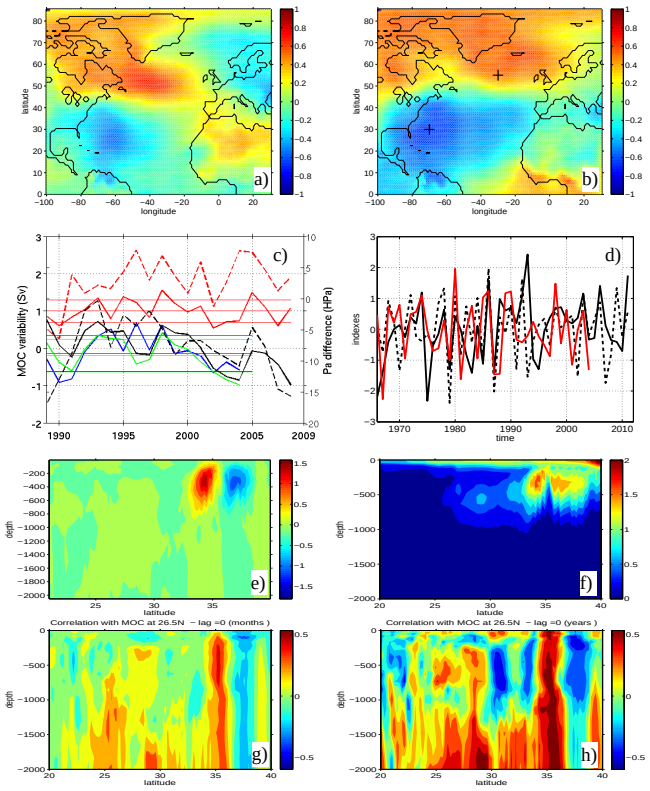

(Caption on next page.)

Fig. 6. Correlation of sea level pressure with ORCA1-ERA **(a)** and ORCA025-ERA **(b)** AMOC-Eks transport for 1989–2008; **(c)** – annual ORCA1-ERA (black), ORCA025-ERA (dashed black), ORCA1-R07 (green) and ORCA025-G70 (blue) AMOC-Eks transports at 26.5° N (in Sv), and January–June mean ΔPa (red, in hPa), see text, and January–June mean NAO^- index (dashed red). Horizontal lines show mean values plus and minus standard deviations (for curves corresponding to the same colours); **(d)** – January–June mean NAO index (black solid), PC1 (red) and annual Gulf Stream north wall index (black dashed); **(e)** – the first leading EOF mode (EOF1) of monthly temperature anomalies at the western boundary; **(f)** – standard deviation of monthly temperature at the western boundary; **(g, h)** – correlations of the AMOC-Ek at 26.5° N with density at the western boundary in ORCA025-G70 for the 45 yr period 1960–2004 inclusive from monthly **(g)** and annual **(h)** data. For figures d-h data after high-pass filtering for periods shorter than 12 months have been used.

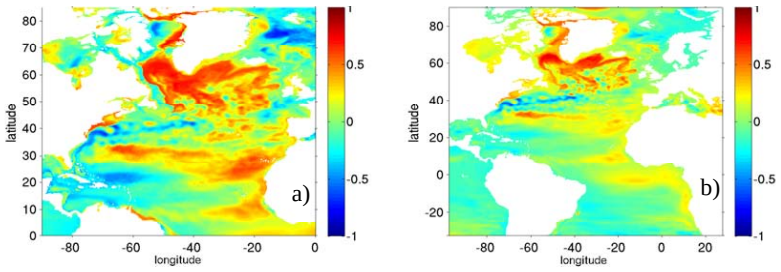

Fig. 7. Correlations of the annual AMOC-Ek at 26.5° N with the top 1000 m averaged density anomalies **(a)** and sea level **(b)** in ORCA025-G70, for the 45 yr period 1960–2004 inclusive; AMOC-Ek variability lags by 4 yr. The correlations between AMOC-Ek and sea level are multiplied by −1.

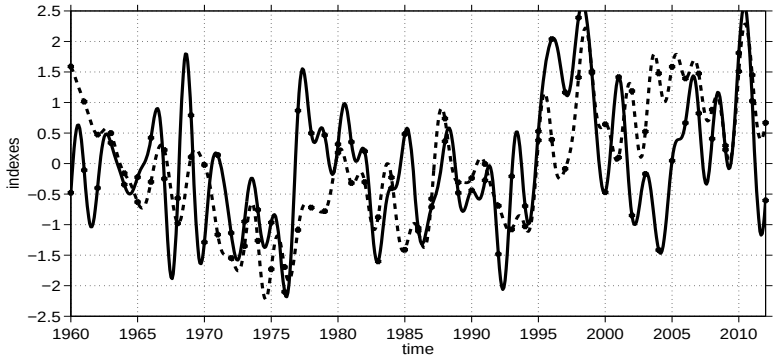

Fig. 8. Normalized NAO-AMOC (solid line, see text) and AMO index (dashed) after low-pass filtering with periods longer than 18 months, stars show January for each year.